Available online at www.sciencedirect.com

SciVerse ScienceDirect

Geochimica et Cosmochimica Acta 114 (2013) 156–168

Geochimica et Cosmochimica Acta

www.elsevier.com/locate/gca

In situ and time resolved nucleation and growth of silica nanoparticles forming under simulated geothermal conditions

Dominique J. Tobler *, Liane G. Benning

Earth and Biosphere Institute, School of Earth and Environment, University of Leeds, LS2 9JT Leeds, UK

Received 19 June 2012; accepted in revised form 17 March 2013; available online 13 April 2013

Abstract

Detailed knowledge of the reaction kinetics of silica nanoparticle formation in cooling supersaturated waters is fundamental to the understanding of many natural processes including biosilicifcation, sinter formation, and silica diagenesis. Here, we quantified the formation of silica nanoparticles from solution as it would occur in geothermal waters. We used an *in situ* and real-time approach with silica polymerisation being induced by fast cooling of a 230 °C hot and supersaturated silica solution. Experiments were carried out using a novel flow-through geothermal simulator system that was designed to work on-line with either a synchrotron-based small angle X-ray scattering (SAXS) or a conventional dynamic light scattering (DLS) detector system. Our results show that the rate of silica nanoparticle formation is proportional to the silica concentration (640 *vs.* 960 ppm SiO_2), and the first detected particles form spheres of approximately 3 nm in diameter. These initial nanoparticles grow and reach a final particle diameter of approximately 7 nm. Interestingly, neither variations in ionic strength (0.02 *vs.* 0.06) nor temperature (reactions at 30 to 60 °C, mimicking Earth surface values) seem to affect the formation kinetics or the final size of the silica nanoparticles formed. Comparing these results with our previous data from experiments where silica polymerisation and nanoparticle formation was induced by a drop in pH from 12 to near neutral (pH-induced, Tobler et al., 2009) showed that (a) the mechanisms and kinetics of silica nanoparticle nucleation and growth were unaffected by the means to induce silica polymerisation (*T* drop or pH drop), both following first order reactions kinetics coupled with a surface controlled reaction mechanism. However, the rates of the formation of silica nanoparticles were substantially (around 50%) slower when polymerisation was induced by fast cooling as opposed to pH change. This was evidenced by the occurrence of an induction period, the formation of larger critical nuclei, and the absence of particle aggregation in the *T*-induced experiments.

1. INTRODUCTION

The polymerisation of aqueous silica leading to the formation of silica nanoparticles occurs in many natural environments (e.g., hot springs, diatoms, marine sediments) and is critical to a variety of processes including biosilicification, biomineralisation, silica diagenesis, or silica sinter formation. Nevertheless, the mechanisms and kinetics by which silica nanoparticles form, grow and aggregate are still fragmented. Several studies investigated the rates of silica polymerisation and precipitation in solutions that mimicked natural fluids (e.g., Iler, 1979; Rothbaum and Rhode, 1979; Rimstidt and Barnes, 1980; Conrad et al., 2007; Tobler et al., 2009 and references therein), thereby obtaining a better understanding of the parameters that control silica saturation in natural waters. In these studies, physico-chemical factors including solution pH, temperature, ionic strength, and silica concentration were shown to heavily

* Corresponding author. Address: Nano - Science Center, University of Copenhagen, Universitetsparken 5, C116, 2100 København Ø, Denmark. Tel.: +45 353 20223; fax: +45 353 20214.

E-mail address: dominique.tobler@nano.ku.dk (D.J. Tobler).

0016-7037/$ - see front matter © 2013 Elsevier Ltd. All rights reserved.
http://dx.doi.org/10.1016/j.gca.2013.03.045

influence the degree of silica saturation and thus the kinetics of silica polymerisation and bulk precipitation.

Despite the fact that these studies have provided us with a basic understanding of how silica polymerises, little research has so far focused on the nucleation and growth kinetics and mechanisms that lead to the formation of nanocolloidal silica particles in supersaturated solutions under conditions that mimic natural waters. These initial steps in the precipitation reaction are however, most important as they determine the size, shape and composition of the nanoparticles, and ultimately define their reactivity (i.e., catalysts; uptake of nutrients/contaminants) and transport behaviour (if the nanoparticles remain in suspension) as well as the ultimate structure and texture of the forming precipitates (e.g., sinters in geothermal waters). For example, sinter growth studies (e.g., Mountain et al., 2003; Handley et al., 2005; Tobler et al., 2008; Tobler and Benning, 2011) indicated that the success and failure of microbial silicification and fossilisation greatly depended on sinter growth rates, and these in turn rely on the quantitative assessment of the kinetics and mechanisms of silica nanoparticle nucleation and growth processes.

So far, most experimental studies on nanocolloidal silica focused on the synthesis of highly monodisperse, spherical and compact silica particles through techniques such as the Stöber method (Stöber et al., 1968). This method uses organic alkoxides precursors as reactants for the production of large quantities of highly size controlled and monodispersed silica nanoparticles for a multitude of industrial application (e.g., biotechnology, catalysis and chromatography). In these alkoxide based synthesis studies, various techniques including small angle X-ray scattering (SAXS), dynamic light scattering (DLS), transmission electron microscopy (TEM), and Raman spectroscopy have been used to derive rates of silica polymerisation and nanoparticle formation (e.g., Halasz et al., 2011; Pabisch et al., 2012). It is however, worth noting that the Stöber method, with its alkoxide-based chemical starting materials and the highly monodispersed final silica nanoparticles, is not representative of silica nanoparticle formation in any natural environment and thus the derived kinetic models are not transferable to any natural processes.

To date, only few attempts were made to quantify the shapes, sizes or kinetics of silica nanoparticles forming in fluids of geologic significance (e.g., Iler, 1979; Rothbaum and Rhode, 1979; Makrides et al., 1980; Conrad et al., 2007; Tobler et al., 2009 and references therein). Amongst these, only our previous study focused on the nucleation and growth kinetics and mechanisms of the silica nanoparticles themselves and used the changes in aqueous silica chemistry (polymerisation rates) primarily as a cross-confirmative measure. In Tobler et al. (2009) we showed that at ambient conditions, when silica supersaturation is induced by a pH change, the nucleation and growth of silica nanoparticles follows three stages: (1) nucleation: characterized by instantaneous homogeneous nucleation of stable critical nuclei with a diameter of 1–2 nm; (2) 3-D growth: characterized by silica nanoparticles growth following first order reaction kinetics coupled with a surface-controlled reaction mechanism; (3) Ostwald ripening and particle aggregation. Stages (1) and (2) are also mirrored by the fast decrease of aqueous silica ([SiO_2 (aq)]) while during stage (3), [SiO_2 (aq)] approaches solubility levels.

In this current study, we build upon our previous work with the aim to better mimic natural systems (e.g., geothermal pools or deep-sea vents) where silica polymerisation and silica nanoparticle formation is the result of cooling (often extremely fast) of a high-temperature, silica supersaturated near-neutral fluid to ambient (geothermal) or low temperatures (deep sea). This is in contrast to most previous studies, where silica polymerisation was most often induced by neutralising a supersaturated, high-pH (usually pH 12 or higher) silica solution to near neutral values in order to bring silica solubility to its minimum (Alexander et al., 1954). A few studies (e.g., Rothbaum and Rhode, 1979; Weres et al., 1981; Carroll et al., 1998) have indicated that silica polymerisation is delayed in systems where silica supersaturation is induced by fast cooling. Up to now, however, a direct comparison and a quantitative assessment of the differences in silica nanoparticle nucleation and growth kinetics and mechanisms between these two approaches are missing. This is mainly due to divergent experimental set-ups used in field *vs.* lab studies (e.g., usage of silica gels, quantifying total silica scale) as well as differences in the evaluation of the reaction kinetics (e.g., precipitation rate as a function of the Gibbs free energy of reaction or as a function of aqueous silica polymerisation rates with varying reaction orders). Furthermore, so far the experimental challenges in mimicking such reactions in the laboratory (e.g., running hydrothermal flow through simulators, controlling the fast cooling while simultaneously monitoring the nucleation/growth kinetics etc.) precluded the quantification of the kinetics and mechanisms of silica nanoparticles formation from cooling hot fluids.

In this current study, we used a flow-through geothermal simulator system that was optimized to operate in conjunction with either a synchrotron-based small angle X-ray scattering (SAXS) system or a conventional flow-through dynamic light scattering (DLS) set-up (Fig. 1). Both these approaches allowed us, independently of each other, to quantify the *in situ* and in real-time nucleation and growth of silica nanoparticles from high temperature solutions. This was done with silica supersaturation being reached through the fast cooling of hot fluids, thus accurately mimicking a natural geothermal system where hot silica supersaturated solutions emerge as springs at the Earth's surface forming amorphous silica sinter deposits (e.g., Carroll et al., 1998; Konhauser et al., 2001; Mountain et al., 2003; Handley et al., 2005; Tobler et al., 2008). In all our experiments the *in situ* scattering data were complemented by aqueous chemical and electron microscopic imaging data, which cross-confirmed the rates, sizes and polydispersity of the nucleating and growing silica nanoparticles. The reactions were monitored for a range of silica concentrations ([SiO_2]), ionic strengths (IS) and temperatures and results were compared to our previous data from experiments where the polymerisation reaction was triggered by a pH-drop (Tobler et al., 2009).

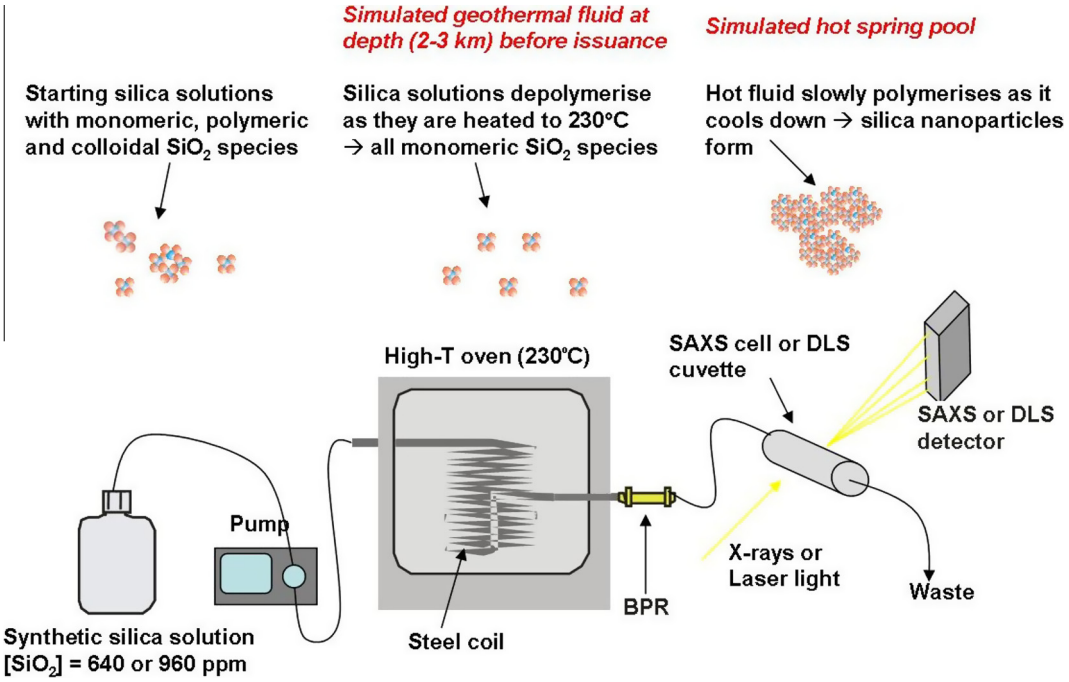

Fig. 1. Schematic diagram of experimental set up to simulate a natural geothermal system where silica nanoparticles form via the fast cooling of a supersaturated monomeric silica solution (modified after Benning and Mountain, 2004). The simulator is interlinked with the *in situ* and real-time scattering cells and detectors.

2. METHODOLOGY

2.1. Experimental set-up and silica nanoparticle synthesis

The flow-through geothermal simulator and the in-line reaction cells/detector systems are illustrated in Fig. 1. A supersaturated solution with a total silica concentration [SiO_2] of either 640 or 960 ppm, and an ionic strength (IS) of 0.02 or 0.06 was prepared at ambient temperatures (25 °C) in a 10 L storage bottle by dissolving specific amounts of $Na_2SiO_3{\cdot}5H_2O$ and NaCl in deionised water. Th pH of these highly alkaline solutions (pH ~12) was then adjusted to 7 using 1 M HCl, and this led to a partly polymerised, near neutral solution (Fig. 1). To run an experiment, these solutions were pumped from the storage bottle into a high-temperature oven (at 230 °C) via a HPLC pump (Fig. 1). Inside the oven, the fluids passed through a 6 m stainless steel coil. The high temperature and the approximately 2.5 h residence time (inside the oven) caused the silica in the circulating fluid to fully de-polymerise, producing a monomeric silica solution (i.e., all silica present as monosilicic acid, [SiO_2(aq)]). This approach mimicked silica-rich fluids in the Earth's crust at about 2–3 km depth and under hydrostatic pressures. After the silica solution passed through the steel coil, it emerged from the oven and passed through a backpressure regulator (BPR) located approximately 15 cm away from the oven exit. This distance assured a temperature drop from 230 to about 80 °C within <1 min. Critically, this induced an increase in silica supersaturation and thus initiated silica polymerisation. This rapid cooling process simulated the conditions when a supersaturated hot fluid is discharged at the Earth's surface (i.e., in a hot spring).

This geothermal simulator allows the *in situ* and time-resolved monitoring of the very first steps of polymerisation and subsequent nucleation and growth of silica nanoparticles within a cooling solution. To monitor these processes the outlet of the BPR is connected to a flow through quartz capillary SAXS cell (1.5 mm OD and 10 μm walls) or a disposable plastic cuvette stationary in the DLS instrument via 1/8 inch Teflon tubing. Once each cell was full, the flow was stopped and data acquisition started (i.e., stopped-flow experiments). The configuration of the SAXS and DLS set-ups allowed measurements to be carried out with simultaneous SAXS data collection only at 30 °C, while DLS measurements were run at final temperatures from 30 to 60 °C. These final temperatures could be achieved by adjusting the tubing length between the backpressure regulator and the SAXS and DLS cell, respectively (i.e., cooling time). Both SAXS and DLS experiments were carried out for up to 3 h with *in situ* monitoring of the changes in the respective scattering properties.

Simultaneously with the SAXS/DLS data collection that monitored the growth of the silica nanoparticles, the polymerisation of the aqueous silica was quantified via the time-dependent change in monosilicic acid concentrations, [SiO_2(aq)], in the reacting solutions. For each experiment, about 5 ml of cooling polymerising solution (collected from the BPR outlet) was analysed over time (up to 2 h) for changes in [SiO_2(aq)] using the spectrophotometric molybdate yellow method (Greenberg et al., 1985).

2.2. Small angle X-ray scattering (SAXS) procedure

All SAXS measurements were carried out at station 6.2 m at the Synchrotron Radiation Source (SRS), Daresbury Laboratory, UK. The parameters that affected the data collection are summarized below and all details about the configuration for station 6.2 m can be found in Cernik et al. (2004).

A wavelength of 1.4 Å and a sample-to-detector distance of 3.75 m were used. Data were collected with a 60° quadrant one-dimensional small-angle detector (gas microgap, multi-wire; Berry et al., 2003; Helsby et al., 2003) and a pair of ion chambers (positioned pre- and post-sample) that monitored the incoming and transmitted beam intensities, respectively. The q-axis was calibrated with the scattering pattern of wet rat-tail collagen.

Time-resolved SAXS spectra were collected every 5 min over 3 h. Due to beam line settings and experimental system operating procedures the first scattering pattern could only be acquired 10 min after the cell was filled with solution (i.e., ~5 min to fill cell, to start SAXS experiments and to secure the hutch; 5 min to acquire the first data point). Data reduction (i.e., correction for detector alinearities, decaying ion beam – using the post-sample ion chamber values, and background scattering) of the 1-D SAXS data was carried out using the program XOTOKO (SRS software packages, Daresbury). The reduced data was further analyzed using GNOM, an indirect transform program for SAXS data processing (Svergun, 1992), to derive information about the size and polydispersity of the growing particles. In the case of a dilute, monodisperse system, GNOM provides an estimate for the radius of gyration, Rg (a shape independent radius) and evaluates a distance distribution function, $p(R\mathrm{g})$. For spherical particles, $p(R\mathrm{g})$ is usually Gaussian shaped (Svergun and Koch, 2003) and Rg is determined from the normalised second moment of the $p(R\mathrm{g})$ curve.

2.3. Dynamic light scattering (DLS)

The DLS experiments were also carried out *in situ* and in a time resolved manner. Data were collected with a Zetasizer Nano ZS (Malvern Instruments) equipped with a He–Ne laser [$\lambda = 633$ nm], and a backscatter detector at a fixed angle of 173°. These settings permit the real-time recording of an intensity autocorrelation function, which is transformed into volume functions to obtain particle size information. In contrast to SAXS, where all experiments were carried out at 30 °C, we used the heating capability of the DLS instruments in order to monitor particle growth (i.e., hydrodynamic particle diameter and polydispersity) also as a function of final temperature, i.e., at 30, 40, 50 and 60 °C.

2.4. Electron microscopy

Silica nanoparticles were imaged either with a field-emission gun scanning electron microscope (FEG-SEM) or a transmission electron microscope (TEM). For FEG-SEM, a few millilitres of a polymerising solution were filtered at specific time intervals through 0.1 μm polycarbonate filters. These were immediately washed with distilled water and left to dry at ambient temperatures. The filter papers were coated with 3 nm platinum and imaged with a LEO 1530 FEG-SEM using a working distance of 3 mm and a beam intensity of 3 kV. TEM samples were prepared by depositing a droplet of the reacting solutions on formvar coated copper grids. The grids were air-dried and imaged using a Philips CM10 TEM at an accelerating voltage of 80 kV.

2.5. Particle size and kinetic analysis

The change in particle radius was evaluated from the radius of gyration, Rg, which is a shape independent radius and is derived from the SAXS data using the computer code GNOM (Svergun, 1992) through a whole pattern fitting algorithm.

Based on our previous work (Tobler et al., 2009) we know that the forming silica nanoparticles are spherical in shape and thus the real particle radius, R, is calculated via (Guinier, 1939):

$$R\mathrm{g}^2 = \frac{3}{5}R^2 \tag{1}$$

The kinetic parameters for the nucleation and growth of the silica nanoparticles (i.e., reaction mechanism, reaction order and rate constant, critical nuclei size) were evaluated from the time-resolved SAXS data using the Chronomal (CM) kinetic model (Nielsen, 1964; Tobler et al., 2009). Full theoretical details about this kinetic model and the specifics about SAXS data analysis are given in Tobler et al. (2009). Briefly, the Chronomal kinetic model is a population-dynamics based kinetic model, which is used in two stages. In a first stage, the experimentally obtained growth profiles (Rg *vs.* time; obtained from GNOM) are converted and normalised to give the degree of reaction, α, ($0 < \alpha \leqslant 1$ with $\alpha = 0$ meaning no scattering above background and $\alpha = 1$ denoting the end of the reaction or no more change in scattering intensity).

$$\alpha = \left(\frac{R\mathrm{g}_t}{R\mathrm{g}^{\max}}\right)^3 \tag{2}$$

where $R\mathrm{g}_t$ is Rg at a given time t, and $R\mathrm{g}^{\max}$ is Rg at the end of the reaction. In a second step, 3 different types of reaction mechanism (chemical, surface, or diffusion controlled) and varying reaction orders are fitted to the normalised reaction profiles in order to obtain the best fit (i.e., highest regression coefficient, R_r^2). From these fits, the critical nuclei radii, R_0, (by extrapolating to $t = 0$), and the reaction rate constants, k are derived (Tobler et al., 2009).

Following our previous approach (Tobler et al., 2009) a second estimate of the critical nuclei size was obtained using the Gibbs–Kelvin approach (Gibbs, 1961):

$$R_0^+ = 2v\sigma/R_cT\ln(S+1) \tag{3}$$

where v is the molar volume (27.2 cm^3; Iler, 1979), σ is the surface energy (for amorphous silica, 80 $\mathrm{erg\,cm}^{-2}$; Iler, 1973), R_c, the gas constant, and S is the supersaturation defined as $S = (C - C_s)/C_s$with C being the actual concentration and C_s the solubility of amorphous silica. Note that previous studies have showed a clear link between solubility and particle size, particularly in crystalline systems such as

TiO_2 and Al_2O_3 nanoparticles (e.g., Navrotsky, 2004; Zhang et al., 2009). Yet, for amorphous silica such data is not available. Here, we used solubility values determined by Gunnarsson and Arnórsson (2000), who determined solubility of amorphous silica but not necessarily silica particles of sizes as studied here. Nevertheless, excellent results from kinetic modelling in our previous study (where we used identical solubility and surface energy values; Tobler et al., 2009) suggested that the chosen values were reasonable.

3. RESULTS AND DISCUSSION

We quantified the kinetics and mechanisms of nucleation and growth of silica nanoparticles *in situ* and in a time resolved manner with the polymerisation being induced by the rapid cooling of a supersaturated silica solution. This way we mimicked silica sinter formation processes in natural geothermal hot springs through experiments conducted with solutions with varying silica concentrations (640 and 960 ppm SiO_2), ionic strengths (0.03 and 0.06 IS) and final temperatures (30–60 °C). These conditions are often the dominant conditions leading to silica sinter formation in major geothermal areas in Iceland or New Zealand (e.g., Mountain et al., 2003; Tobler et al., 2008 and references therein).

3.1. Silica polymerisation: [SiO_2(aq)] over time

Silica polymerisation is the process where monosilicic acid, [SiO_2(aq)], coalescence to polymeric chains which eventually form 3D internally-condensed, yet highly hydrated nanometer sized spherical particles (Iler, 1979). In Fig. 2, the time dependent decrease in [SiO_2(aq)] as a function of initial silica concentration (640 and 960 ppm SiO_2), ionic strength (0.03 and 0.06 IS) and final temperature (30–60 °C) is shown. Time zero corresponds to the point in time when the final temperature was reached, i.e., silica supersaturation no longer increased (2–3 min after start of cooling). Note that at time zero less than 4% of the monosilicic acid polymerised as shown by [SiO_2(aq)] values close to the initial SiO_2 concentration for all tested conditions (Fig. 2). Fig. 2A reveals that the initial silica concentration and thus the degree of silica supersaturation had a major impact on the rate of silica polymerisation: the depletion of [SiO_2(aq)] in the 960 ppm SiO_2 experiment is markedly faster compared to the polymerisation in the 640 ppm experiment. Starting close to 960 ppm about 75% of the monosilicic acid polymerised within the first 20 min (with respect to amorphous silica solubility at 30 °C; dotted line in Fig. 2A), whereas only 28% polymerised at lower [SiO_2]. In contrast, ionic strength had little to no effect on the overall decrease of [SiO_2(aq)] over time. Note that in all three data sets polymerisation rates considerable decreased after 1 h. Although

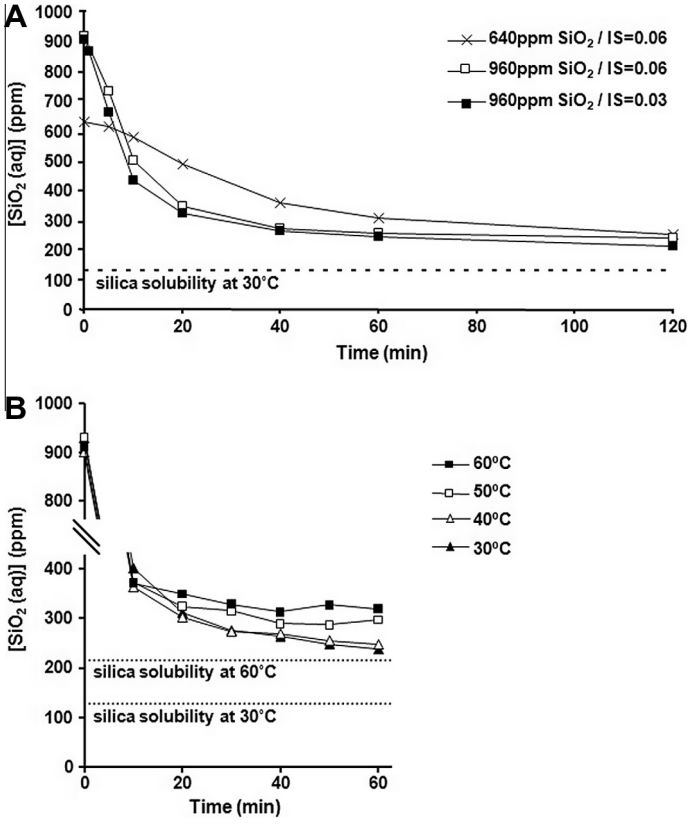

Fig. 2. Time-dependent decrease in monosilicic acid concentrations, [SiO_2(aq)], as a function of (A) initial silica content (640 *vs.* 960 ppm SiO_2) and ionic strength (0.03 *vs.* 0.06 IS) at 30 °C and (B) in experiments with 960 ppm SiO_2 and 0.03 IS with varying final temperatures (30–60 °C). Dotted lines represent amorphous silica solubility in solutions with IS = 0.03 (based on Gunnarsson and Arnórsson, 2000).

measurements were stopped after 2 h, it is expected that the aqueous silica would continuously decrease over the following days slowly approaching the amorphous silica solubility at 30 °C. This has been demonstrated in previous studies on silica polymerisation, where a decrease in aqueous silica was observed for up to 20 days after supersaturation was reached (e.g., Iler, 1979; Carroll et al., 1998; Conrad et al., 2007).

The effect of temperature (30–60 °C) on the polymerisation process for solutions with 960 ppm SiO_2 and IS = 0.03 (Fig. 2B) showed that again within the first 20 min, and regardless of final temperature, approximately 80% of the initial [SiO_2(aq)] polymerised, reaching ~360–400 ppm. Thereafter, the polymerisation process proceeded considerably slower. As expected from the higher supersaturation at lower temperature, comparison of the 30 and 60 °C profiles showed that polymerisation occurred faster at 30 °C (dotted lines in Fig. 2B).

3.2. Silica nanoparticle growth: SAXS

The typical time-resolved change in the SAXS patterns during an *in situ* experiment (Fig. 3) revealed that with increasing time the total scattering intensity, $I(q)$, and the slope at low q of the scattering curve increased. An increase in $I(q)$ indicates an increase in electron density contrast between matrix and the newly formed particles but also an increase in total scattering volume (i.e., increase in particle volume or number). The increase in slope at low q (Guinier region, $qRg < 1$; Guinier, 1939) indicates an increase in particle size with time.

GNOM analyses of the SAXS pattern yielded best results when choosing a monodisperse system as opposed to a polydisperse system. GNOM derived Rg values (radius of gyration) were converted to particle radius, R, using Eq. (1), and then illustrated as a function of time at different silica concentrations and ionic strengths in Fig. 4A. Comparison of growth profiles at high [SiO_2] (960 ppm) but at different IS (0.03 *vs.* 0.06) showed an identical behaviour with time. The first scattering pattern (10 min) revealed particles with a radius of ~1.5 nm and over the 3 h of the experiment the radius increased and approached a plateau at approximately 3.5 nm. In contrast, particle growth was significantly delayed in the experiment at lower [SiO_2] (640 ppm, 0.06 IS; Fig. 4A crosses), and particles were only observed after about 60 min. Again, the first particles had a radius of approximately 1.5 nm, and they steadily increased in size over the following 2 h. At this lower [SiO_2], however, even after 3 h a plateau in the growth profile and thus a stable particle size was not observed. Extrapolation of the growth curve to a plateau suggested that the time to reach the end of particle growth at this concentration was significantly longer (possibly up to 6 h, Fig. 4A). The presence of an induction time suggests that formation of stable nuclei and subsequent particle growth only occurred after a certain degree of polymerisation was reached. Furthermore, the SAXS experimental and beam line configuration and the small difference between background and the first scattering pattern (signal to noise issues) might have limited our data quality to analysis of particles with radii $\geqslant$1.5 nm. It is thus likely that with the approach and set-up used here we were not able to monitor the nucleation of critical nuclei. Overall, our SAXS results agreed with the time-dependent decrease in monosilicic acid concentrations (Fig. 2A) and reaffirmed that the initial [SiO_2] (i.e., silica supersaturation) was the prime control for the rate of silica polymerisation and nanoparticle growth, while the differences in IS did not cause detectable deviations.

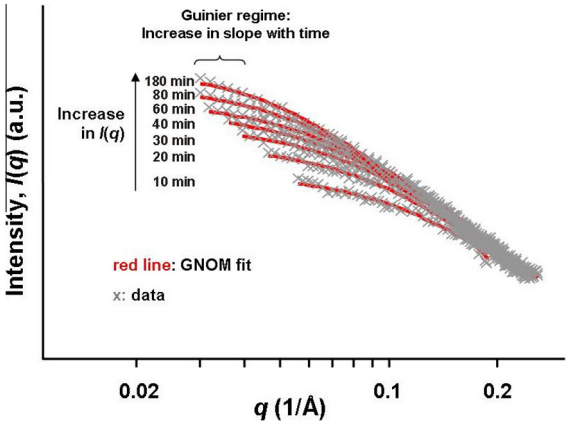

Fig. 3. Log–log plot of the scattering intensity as a function of scattering angle and time (960 ppm SiO_2, 0.03 IS, 30 °C). Note that SAXS patterns were collected every 5 min (up to 3 h) but for clarity only a few patterns are shown. The errors for each data point are smaller than the symbols (<3%).

The second parameter evaluated with GNOM was the distance distribution function, $p(R)$ (where Rg was converted to R using Eq. (1)). The increase in both the area under the curve and the apex of the curve indicated an increase in particle size. The near-Gaussian shape of the $p(R)$ suggested fairly monodisperse and spherical silica nanoparticles. The observed slight skew to the right and the tails at higher R is due to the presence of some aggregates or a certain degree of polydispersity. Note that the shape and evolution of the $p(R)$ curves did not differ between experiments (i.e., over the studied SiO_2/IS) and all $p(R)$ plots were slightly skewed towards the right.

3.3. Silica nanoparticle growth: DLS

The time-resolved DLS data shows the time-dependent change in the scattering of laser light caused by the Brownian motion of the forming silica particles which is related to changes in the apparent mean hydrodynamic diameter of the growing particles (Fig. 5). The large scatter in the data with the errors reaching 36% is due to the low resolution of DLS at small particle sizes (Fig. 5; as compared to the 1–3% error for the SAXS data). Nevertheless, the particle growth rate *vs.* [SiO_2]/IS trends are comparable to those observed with SAXS (Fig. 4). In the 960 ppm SiO_2 experiment, silica nanoparticles with a hydrodynamic diameter of approximately 3 nm formed shortly after the measurements were initiated (16 min). This diameter matched perfectly with the 1.5 nm radius derived from the first SAXS pattern (10 min, Fig. 4A). In contrast, at lower [SiO_2] (640 ppm, Fig. 5A), it took about 40 min for the first DLS patterns

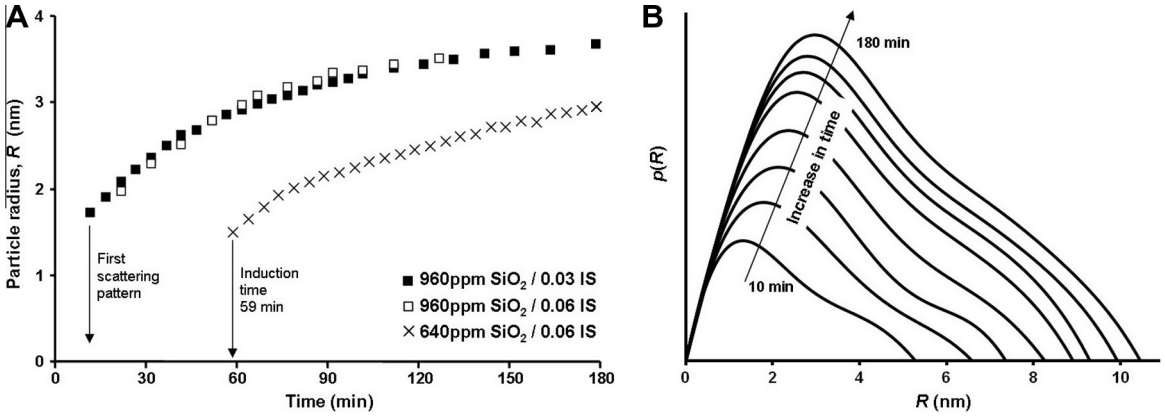

Fig. 4. (A) Time course of particle radius (R, in nm) in solutions with 640 ppm and 960 ppm SiO_2 and different IS (errors smaller than symbols; ~3%). (B) Example of a distance distribution function $p(R)$ plot for the scattered silica nanoparticles as a function of radius, R, and time (960 ppm SiO_2, 0.03 IS).

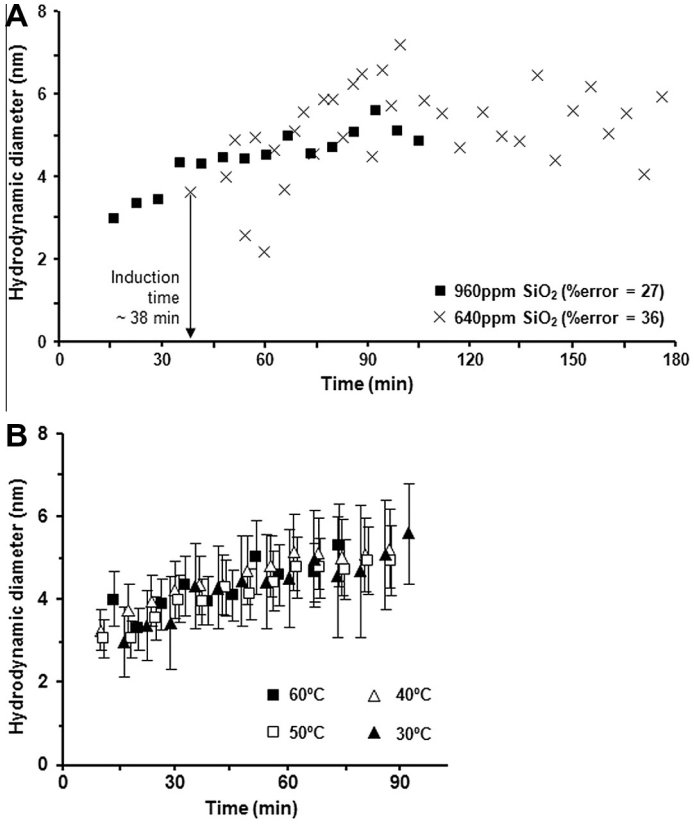

Fig. 5. (A) Hydrodynamic diameters of growing silica nanoparticles in solutions that had a final temperature of 30 °C evaluated from the DLS volume data. The arrow indicates the induction period (i.e., first detectable particle) for the 640 ppm SiO_2 experiment (% errors are average values for each experiment). (B) DLS growth profiles for silica nanoparticles formed in a solution with 960 ppm SiO_2 and 0.03 IS that had reached various final temperatures.

to reveal scatter above background. Despite the far lager errors of DLS compared to SAXS, this is a ~20 min shorter induction time compared to the SAXS results (Fig. 4A).

The time-dependent decrease in aqueous silica showed slightly higher polymerisation rates at lower T (Fig. 2B), thus a faster growth rate was expected at 30 °C compared to 60 °C. However, DLS measurements at various final temperatures (30–60 °C) revealed no detectable effect of temperature on particle size or growth rate (Fig. 5B). In all growth profiles, the first detectable particles had a diameter of around 3 nm which then increased to about 5 ± 1 nm within the first 90 min. This is likely due to the larger errors of the DLS data which make a further evaluation of absolute differences impractical.

Taken together, the SAXS and DLS results both confirmed our previous study which showed that the rates of silica polymerisation and nanoparticle formation were affected by increasing silica concentration (Tobler et al., 2009; supersaturation reached at 25 °C and through a pH drop). Our previous results further demonstrated that a change in ionic strength affected the silica solubility and thus the polymerisation reaction and particle growth rate. However, in the current study (where supersaturation was reached by a fast temperature drop from 230 °C) the variations in tested IS (0.03 *vs.* 0.06) as well as T (30–60 °C) showed no effect on nanoparticle formation or the differences could not be resolved with the techniques applied in this study.

3.4. Silica nanoparticle imaging/size analysis: electron microscopy

The particle sizes obtained from SAXS and DLS were verified by imaging of the resulting particles at various time steps. After 3 h of polymerisation in a solution with 960 ppm SiO_2 and IS = 0.03 tiny but rounded particles and particle aggregates (Fig. 6A) were observed. Although a rough particle size could be derived, the FEG-SEM resolution was too low to obtain accurate measurements. A more accurate particle size value was derived from TEM photomicrographs (Fig. 6B) where the individual particles confirmed the spherical shape and fairly monodisperse size distribution observed with SAXS. The average particle diameters and the polydispersity (i.e., standard deviation) was determined from samples quenched and imaged at two aging times (2 and 3 h) and results are listed in the table of Fig. 6 along with SAXS and DLS data for comparison. The data revealed that the sizes derived from the TEM images were significantly smaller (up to 50%) than those derived from DLS and SAXS. This was not unexpected as for TEM analyses samples were dried and placed under high vacuum and thus the amorphous silica nanoparticles underwent dehydration and relaxation. This caused the highly hydrous and open-structured particles to collapse and aggregate as compared to SAXS and DLS where silica nanoparticles were examined in their native/hydrated state (Tobler et al., 2009).

3.5. Reaction kinetics of silica nanoparticle formation

In all experiments, the reacting solutions were supersaturated with respect to amorphous silica and particle nucleation was assumed to be homogeneous and instantaneous (Tobler et al., 2009). Upon reaching the desired temperature at high [SiO_2], silica nanoparticles nucleated almost instantaneously (i.e., maximum 1 min after SAXS measurements were started) as indicated by the fast decrease in aqueous silica (Fig. 2A). This was corroborated by the excellent fit of the normalised SAXS data to the Chronomal kinetic model (regression coefficient, R_r^2, = 0.99; Fig. 7) which assumes instantaneous nucleation. In contrast, at lower supersaturation (640 ppm SiO_2) both SAXS and DLS results revealed that nucleation was preceded by an induction period, and thus at lower silica concentration nucleation was not instantaneous. This was due to the delayed polymerisation reaction as shown by the slow decrease in monosilicic acid concentration in Fig 2A. The absence of instantaneous nucleation and an incomplete particle growth profile (i.e., even after 3 h a final particle size was not reached) prohibited a fitting of the 640 ppm SiO_2 SAXS data to the Chronomal model.

From the first SAXS pattern (10 min after 30 °C and final supersaturation was reached) particles with radii of ~1.5 nm were derived. At the time of our experiments beam

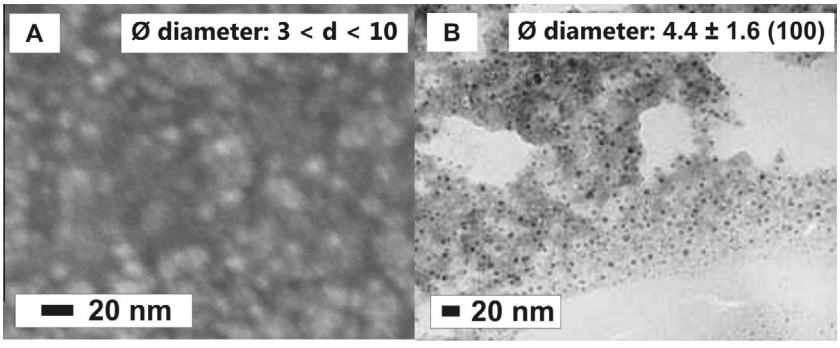

SiO_2 (ppm)	IS	Time (h)	Particle diameter (nm)		
			SAXS	DLS	TEM
960	0.03	2	6.8 ± 0.2	5.7 ± 2.9	3.2 ± 0.6
		3	7.3 ± 0.2	6.6 ± 3.3	4.4 ± 1.6

Fig. 6. (A) FEG-SEM image (white spots = particles) and (B) TEM image (black spots = particles) of silica nanoparticles grown for 3 h in a solution with 960 ppm SiO_2 and IS = 0.03. Table shows comparison of particle diameters obtained from SAXS, DLS and TEM.

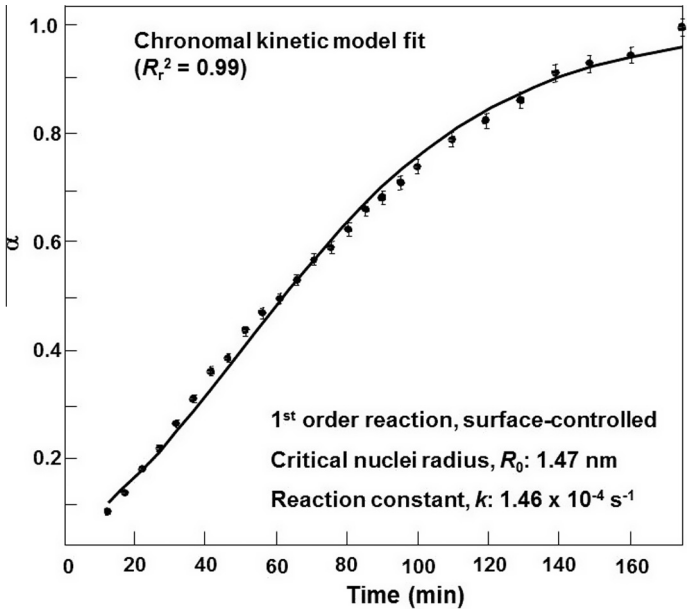

Fig. 7. Reaction process, α (Eq. (2)), for the 960 ppm SiO_2/0.03 IS experiment. The solid line represents the fit to the Chronomal kinetic model from which the kinetic parameters were derived.

line configurations and low signal to noise issues prevented us from collecting patterns immediately after the start of the experiments and thus the first measured particle radii do not represent critical nuclei sizes. Nevertheless, the critical nuclei sizes could be estimated via two procedures, i.e., using the Gibbs–Kelvin equation and from Chronomal modelling. It is worth noting that in our previous study on silica nanoparticle formation in pH-induced systems (Tobler et al., 2009) we obtained excellent agreement in critical nuclei size between these two procedures. Under the conditions tested here, the Gibbs–Kelvin critical nuclei, R_0^+ (calculated using Eq. (3)), was not affected by ionic strength but was considerably smaller in 960 ppm SiO_2 experiments ($R_0^+ = 0.85$ nm) compared to 640 ppm SiO_2 experiments ($R_0^+ = 1.07$ nm). This was not unexpected as the nucleation process has a higher driving force in more supersaturated solutions thus enabling the formation and stabilisation of many but smaller nuclei (Lasaga, 1998). The second estimate of the critical nuclei radii for the 960 ppm SiO_2/0.03 IS experiment was obtained from the excellent fit between data and the Chronomal kinetic model (Fig. 7). The results revealed a critical nucleus of $R_0 = 1.47$ nm which was considerably larger than the R_0^+ value from the Gibbs–Kelvin approach (0.85 nm). This discrepancy was somewhat surprising as excellent agreement was obtained in our previous study (Tobler et al., 2009). The fact that the Gibbs–Kelvin approach accounts solely for the degree of supersaturation, but does not consider other parameters (e.g., induction time, presence of salts etc.) may influence the critical nuclei size evaluation. In contrast, for Chronomal analysis, the full particle growth is fitted and the extrapolation to time 0 may be more representative for R_0.

The nucleation stage was followed by the fast decrease of monosilicic acid (Fig. 2) and the 3-dimensional growth of silica nanoparticles (Fig. 4A). The spherical shape and the fairly monodisperse distribution of the silica particles was verified by SEM and TEM (Fig. 6) and also by the good fit of the SAXS data to the Chronomal model (which assumes 3-D, classical growth, Fig. 7). The Chronomal analysis further showed that particle growth obeyed a first order rate law with a surface-controlled mechanism which matches our previous results where silica polymerisation and nanoparticle formation was induced through a drastic pH change. Several previous studies suggested that Ostwald ripening (OR) and particle aggregation are the dominant processes in the later stages of silica nanoparticle formation (e.g., Iler, 1979; Perry and Keeling-Tucker, 2000; Tobler et al., 2009). At both tested SiO_2 concentration, we were not able to capture full particle growth profiles which made fitting to LSW theory (Lifshitz and Slyozov, 1961; Wagner, 1961) to test for the occurrence of OR impractical. Moreover, the DLS measurements, which are highly susceptible to the presence of even a small proportion of large aggregates (i.e., 1–2% by volume; see Tobler et al., 2009), clearly showed that aggregation did not occur over the monitored time frame. This does however, not exclude the occurrence of OR and particle aggregation at a later stage of these experiments, after SAXS and DLS measurements were terminated.

3.6. How do silica nanoparticles form in natural settings: *T- vs.* pH-induced process

The prime aim of this study was to quantify the kinetics and mechanisms of the nucleation and growth of silica nanoparticles under conditions that mimic primarily processes in natural geothermal systems – i.e., by a drastic change in temperature upon emergence of the fluids at the Earth's surface. Furthermore, we wanted to show how a

combination of *in situ* and time resolved scattering measurements can be used to derive highly accurate data sets pertinent to silica particle nucleation, data sets that could be compared to the vast majority of previous experiments that quantified silica nanoparticle growth through a less realistic dramatic pH drop method (e.g., Alexander et al., 1954; Iler, 1979; Tobler et al., 2009 and references therein). The "pH-induced" method has been so far the most practical in terms of experimental approaches, but it is however, not representative of the processes occurring in natural geothermal systems, where the polymerisation reaction is a result of rapid cooling of supersaturated, most often near-neutral, high temperature fluids ('*T*-induced'). In solutions with identical composition, it is expected that the polymerisation reaction and thus silica nanoparticle growth would be similar, regardless of the induction process. The few previous studies that focused on silica polymerisation and precipitation in natural geothermal waters and/or simulated natural geothermal processes (e.g., Rothbaum and Rhode, 1979; Weres et al., 1981; Carroll et al., 1998) had demonstrated that silica polymerisation is delayed when polymerisation is induced by fast cooling (compared to pH-induced). However, we are still lacking an understanding of how silica nanoparticle nucleation rates and mechanism are affected by this. In our previous study (Tobler et al., 2009) we have however, quantified the formation of silica nanoparticles using pH-induced method while applying the same set of techniques and similar solution chemistries as in the current study. With the current new data set we are now in the position to compare silica polymerisation and silica nanoparticle formation using almost identical solution compositions but from a '*T*-induced' (current study: 640 ppm SiO_2 and IS = 0.06) and a 'pH-induced' (Tobler et al., 2009: 640 ppm SiO_2 and IS = 0.02) approach. This way we can assess if mode of induction of silica polymerisation is affecting the mechanisms and/or kinetics of silica polymerisation and nanoparticle formation (*T- vs.* pH-induced). This comparison is summarised in Fig. 8 and Table 1 and discussed below. Note that the slight difference in IS between the two data sets (0.02 IS in pH-induced *vs.* 0.06 IS in *T*-induced experiment, Fig. 8) could be neglected as shown by results discussed above (Fig. 4A).

The dominant trend observed in Fig. 8 shows that the polymerisation and particle growth proceeded faster when the reaction was induced by a change in pH (rate constant >50% larger, Table 1). This is visible through the instantaneous decrease in $[SiO_2(aq)]$ and the simultaneous increase in particle size in the pH-induced experiment, compared to the considerably delayed polymerisation and particle growth in the *T*-induced experiment (Fig. 8). This was corroborated by the considerably higher Chronomal rate constant for particle growth in the pH-induced

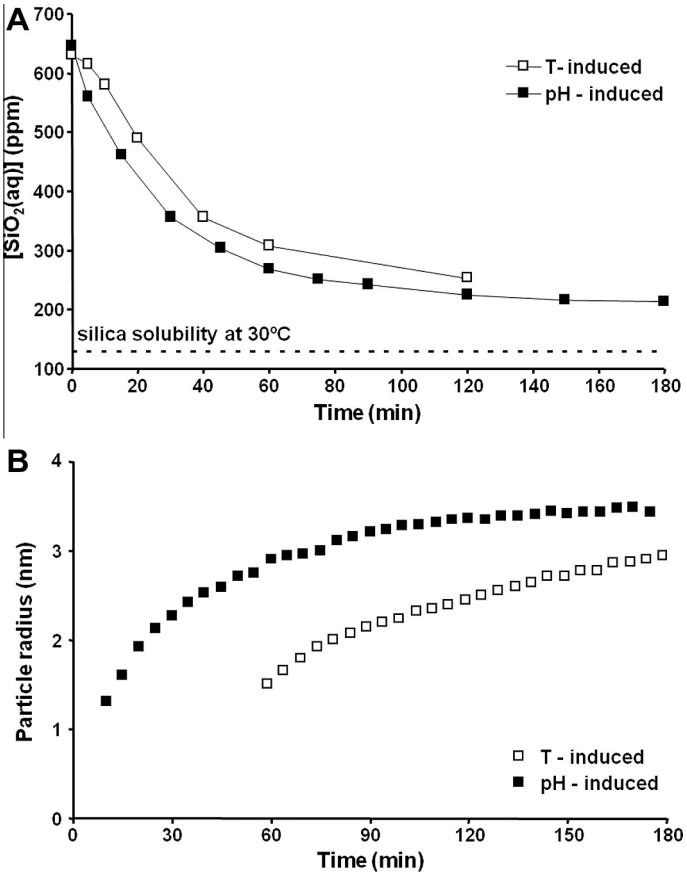

Fig. 8. The effect of *T*- and pH-induced silica supersaturation on (A) the time-dependent depletion in $[SiO_2(aq)]$ and (B) the increase in SAXS particle radius over time in solutions with 640 ppm SiO_2 (at 30 °C).

Table 1
Comparison between the derived kinetic parameters for the pH- and T-induced experiments for solutions with initial 640 ppm SiO_2.

	pH-induced	T-induced
Nucleation		
R_0^+ Gibbs–Kelvin approach	1.07	1.07
R_0 Chronomal Analysis	1.09	–
Induction period	No	~60 min
Particle growth		
1st order reaction, surface-controlled	Yes	Yes[a]
Chronomal rate constant ($\times 10^{-4}$ s^{-1})	5.13	<1.46[b]
Aggregation		
DLS	Yes	No

[a] Assuming particle growth mechanism is not affected by SiO_2 concentration.
[b] Chronomal kinetic parameters from 960 ppm SiO_2 experiment.

($k = 5.13 \times 10^{-4}$ s^{-1}) compared to the T-induced experiment ($k < 1.46 \times 10^{-4}$ s^{-1}). Although in the T-induced experiments k was obtained from the high [SiO_2] (960 ppm) experiment, at 640 ppm [SiO_2], however, a smaller rate constant would be expected. Lastly, in the pH-induced experiments (Tobler et al., 2009) we had observed particle aggregation while in the T-induced experiments in the current study no particle aggregation was observed. Nevertheless, the important observation is that the growth mechanism is not affected by the mode of achieving supersaturation and both pH- and T-induced polymerisation lead to a 1st order, surface-controlled growth of the silica nanoparticles.

Following the differences in reaction rates, it would be expected that the two different approaches also yielded different sized critical nuclei. Here, no Chronomal critical nuclei size could be obtained for the T-induced 640 ppm SiO_2 experiment, but it could be estimated using the Gibbs–Kelvin equation. Not surprisingly however, identical Gibbs–Kelvin critical nuclei sizes were calculated for the pH and T-induced system (Table 1) as this equation is only dependent on the degree of supersaturation and does not account for the rate at which supersaturation is established. In the T-induced experiment, where the reaction was significantly slower than in the pH-induced experiment (Fig. 8, Table 1), a larger critical nuclei would, however, be expected (Lasaga, 1998). This suggests that the critical nuclei in the T-induced system were probably larger than what was estimated using the Gibbs–Kelvin equation (>1.07 nm). This may also explain the discrepancy in critical nuclei size between values determined with the Gibbs–Kelvin equation and with the Chronomal model for the 960 ppm SiO_2 experiment (see Section 3.6), Moreover, it indicates that in this particular study the Gibbs–Kelvin equation underestimates the critical nuclei size and the extrapolation of the growth curve to time zero (using the Chronomal model) thus provides a more accurate estimate of the critical nuclei size.

The >50% slower rates of silica polymerisation and particle growth and the larger critical nuclei size in current T-induced experiments is explained by the differences in time to establish supersaturation. In the pH-induced experiments, the sudden change in pH from 12 to 7 (<30 s) induced instantaneous supersaturation and thus forced the monosilicic acid to polymerise. In contrast, the cooling process of the hot fluids (emerging from the high-T oven) from 230 to 30 °C took 2 to 3 min. This led to a more gradual increase in supersaturation (as T decreased) and thus slower rates of silica polymerisation. In addition, the pH- and T-dependency of silica solubility differ substantially. With regards to pH, silica solubility is at a minimum around pH 6–9 but then increases drastically at pH > 9 (Alexander et al., 1954). In the case of temperature, the solubility does not exhibit any dramatic changes but steadily increases with increasing T (Gunnarsson and Arnorsson, 2000). Thus the radical change in pH imposed a faster attainment of supersaturated conditions and thus the polymerisation reaction was substantially faster compared to the polymerisation induced by the gradual change in T, which also explains the differences in reaction rates and critical nuclei sizes.

Results from this study are critical to the understanding of a variety of natural processes. For example, microbial silicification and fossilisation have been widely investigated in laboratory studies to determine the geochemical conditions for optimal microbial preservation in ancient and modern silica sinters (e.g., Yee et al., 2003; Benning et al., 2004a,b; Lalonde et al., 2005 and references therein). In most of these experiments, silica polymerisation and precipitation were induced by a change in pH. Therefore it is likely that the reported optimal silicification conditions may need to be reconsidered in light of the new results presented here. Moreover, energetic considerations and geochemical modelling of other processes that involve silica nanoparticle formation from cooling supersaturated waters (e.g., sinter formation, silica diagenesis) need to be adjusted to account for lower polymerisation and precipitation rates shown in this study. Comparisons with natural silicification and sinter growth experiments carried out in modern active geothermal pools (i.e., Mountain et al., 2003; Tobler et al., 2008) showed that silica precipitation and microbial silicification is highly dependent on supersaturation and polymerisation rates but that in natural settings salt content and the organic compounds of microbial systems also highly affect silicification rates.

The kinetics of the nucleation, growth and aggregation of silica nanoparticles in cooling waters have also direct implication for industrial processes. For example, silica precipitation and scaling at geothermal power plants is a well known problem. Accurate knowledge of rates of silica polymerisation and silica nanoparticle formation in cooling silica supersaturated waters is thus critical to predict the level of silica scaling that can be expected in cooling geothermal waters. Equally, this data can help to optimise handling strategies for the fast cooling geothermal water to reduce silica scaling in key positions such as pipelines and injection wells.

Importantly, however, this study also showed that our newly developed high-temperature system run in-line with time resolved aqueous analyses and *in situ* and time resolved particle formation and these particle property measurements have now lead to a more accurate picture of a nucleation and growth process of silica nanoparticles.

These results are highly relevant to our understanding of modern and ancient silica sinter formation processes both on Earth and potentially elsewhere.

ACKNOWLEDGEMENTS

The authors thank Christopher Martin for beamtime and technical assistance to carry out SAXS measurements at station 6.2 m at the Synchrotron Radiation Source (SRS), Daresbury Laboratory, UK. Financial support via a PhD fellowship for DJT from the Earth and Biosphere Institute (University of Leeds, UK), and research funds for LGB from the University of Leeds are acknowledged.

REFERENCES

Alexander G. B., Heston W. M. and Iler R. K. (1954) The solubility of amorphous silica in water. *J. Phys. Chem.* **58**, 453–455.

Benning L. G. and Mountain B. M. (2004) The silicification of microorganisms: a comparison between in situ experiments in the field and laboratory. In *Water–Rock Interaction* (eds. Wanty and Seal). Taylor and Francis Group, London, pp. 3–10.

Benning L. G., Phoenix V. R., Yee N. and Konhauser K. O. (2004a) The dynamics of cyanobacterial silicification: an infrared micro-spectroscopic investigation. *Geochim. Cosmochim. Acta* **68**, 729–741.

Benning L. G., Phoenix V. R., Yee N. and Tobin M. J. (2004b) Molecular characterization of cyanobacterial silicification using synchrotron infrared micro-spectroscopy. *Geochim. Cosmochim. Acta* **68**, 743–757.

Berry A., Helsby W. I., Parker B. T., Hall C. J., Buksh P. A., Hill A., Clague N., Hillon M., Corbett G., Clifford P., Tidbury A., Lewis R. A., Cernik B. J., Barnes P. and Derbyshire G. E. (2003) The RAPIP2 x-ray detection system. *Nucl. Instrum. Methods Phys. Res., Sect. A* **513**, 260–263.

Carroll S., Mroczek E., Alai M. and Ebert M. (1998) Amorphous silica precipitation (60 to 120 degrees C): comparison of laboratory and field rates. *Geochim. Cosmochim. Acta* **62**, 1379–1396.

Cernik R. J., Barnes P., Bushnell-Wye G., Dent A. J., Diakun G. P., Flaherty J. V., Greaves G. N., Heeley E. L., Helsby W., Jaques S. D. M., Kay J., Rayment T., Ryan A., Tang C. C. and Terrill N. J. (2004) The new materials processing beamline at the SRS Daresbury, MPW6.2. *J. Synchrotron Radiat.* **11**, 163–170.

Conrad C. F., Yasuhara H., Bandstra J. Z., Icopini G. A., Brantley S. L. and Heaney P. J. (2007) Modeling the kinetics of silica nanocolloid formation and growth in aqueous solutions as a function of pH and ionic strength. *Geochim. Cosmochim. Acta* **71**, 531–542.

Gibbs W. (1961). .

Greenberg A. E., Trussell R. R. and Clesceri L. (1985) *Standard Methods for the Examination of Water and Wastewater*. , 209 pp.

Guinier A. (1939) La diffraction des rayons X aux tres petits angles: application al'étude de phénomenes Ultramicroscopiques. *Ann. Phys.* **12**, 161–237.

Gunnarsson I. and Arnórsson S. (2000) Amorphous silica solubility and the thermodynamic properties of H_4SiO_4 in the range of 0° to 350°C at P_{sat}. *Geochim. Cosmochim. Acta* **64**, 2295–2307.

Halasz I., Kierys A., Goworek J., Liu H. M. and Patterson R. E. (2011) (29)Si NMR and Raman glimpses into the molecular structures of acid and base set silica gels obtained from TEOS and Na-silicate. *J. Phys. Chem. C* **115**, 24788–24799.

Handley K. M., Campbell K. A., Mountain B. W. and Browne P. R. L. (2005) Abiotic–biotic controls on the origin and development of spicular sinter: in situ growth experiments, Champagne Pool, Waiotapu, New Zealand. *Geobiol.* **3**, 93–114.

Helsby W. I., Berry A., Buksh P. A., Hall C. J. and Lewis R. A. (2003) The RAPID2 interpolating system. *Nucl. Instrum. Methods Phys. Res., Sect. A* **510**, 138–144.

Iler R. K. (1973) Colloidal silica. In *Surface and Colloid Science* (ed. E. Matijevic). Wiley Interscience & Plenum Publisher.

Iler R. K. (1979) *The Chemistry of Silica*. John Wiley, New York.

Konhauser K. O., Phoenix V. R., Bottrell S. H., Adams D. G. and Head I. M. (2001) Microbial–silica interactions in Icelandic hot springs sinter: possible analogues for some Precambrian siliceous stromatolites. *Sedimentology* **48**, 415–433.

Lalonde S. V., Konhauser K. O., Reysenbach A. L. and Ferris F. G. (2005) The experimental silicification of Aquificales and their role in hot spring formation. *Geobiology* **3**, 41–52.

Lasaga A. C. (1998) *Kinetic Theory in the Earth Sciences*. Princeton University Press, Princeton, New Jersey, 811 p.

Lifshitz I. M. and Slyozov V. V. (1961) The kinetics of precipitation from supersaturated solid solutions. *J. Phys. Chem. Solids* **19**, 35–50.

Makrides A. C., Turner M. and Slaughter J. (1980) Condensation of silica from supersaturated silicic acid solutions. *J. Colloid Interface Sci.* **73**, 345–367.

Mountain B. W., Benning L. G. and Boerema J. (2003) Experimental studies on New Zealand hot spring sinters: rates of growth and textural development. *Can. J. Earth Sci.* **40**, 1643–1667.

Navrotsky A. (2004) Energetic clues to pathways to biomineralization: precursors, clusters, and nanoparticles. *PNAS* **101**, 12096–12101.

Nielsen A. E. (1964) Kinetics of precipitation. In *International Series of Monographs on Analytical Chemistry* (eds. R. Belcher and L. Gordon). Pergamon Press, Oxford, UK.

Pabisch S., Feichtenschlager B., Kickelbick G. and Peterlik H. (2012) Effect of interparticle interactions on size determination of zirconia and silica based systems – a comparison of SAXS, DLS, BET, XRD and TEM. *Chem. Phys. Lett.* **521**, 91–97.

Perry C. C. and Keeling-Tucker T. (2000) Biosilicification: the role of the organic matrix structure control. *J. Biol. Inorg. Chem.* **5**, 537–550.

Rimstidt J. D. and Barnes H. L. (1980) The kinetics of silica–water reactions. *Geochim. Cosmochim. Acta* **44**, 1683–1699.

Rothbaum H. P. and Rhode A. G. (1979) Kinetics of silica polymerisation and deposition from dilute solutions between 5 and 180°C. *J. Colloid Interface Sci.* **71**, 533–559.

Stöber W., Fink A. and Bohn E. (1968) Controlled growth of monodisperse silica spheres in the micron size range. *J. Colloid Interface Sci.* **26**, 62–69.

Svergun D. I. (1992) Determination of the regularization parameter in indirect-transform methods using perceptual criteria. *J. Appl. Cryst.* **25**, 495–503.

Svergun D. I. and Koch M. H. J. (2003) Small-angle scattering studies of biological macromolecules in solution. *Rep. Prog. Phys.* **66**, 1735–1782.

Tobler D. J. and Benning L. G. (2011) Bacterial diversity in five Icelandic geothermal waters: temperature and sinter growth rate effects. *Extremophiles* **15**, 473–485.

Tobler D. J., Stefánsson A. and Benning L. G. (2008) In-situ grown silica sinters in Icelandic geothermal areas. *Geobiology* **6**, 481–502.

Tobler D. J., Shaw S. and Benning L. G. (2009) Quantification of initial steps of nucleation and growth of silica nanoparticles: an

in-situ SAXS and DLS study. *Geochim. Cosmochim. Acta* **73**, 5377–5393.

Wagner C. (1961) Theorie der Alterung von Niderschlagen durch Umlosen (Ostwald Reifung). *Z. Electrochemie* **65**, 581–591.

Weres O., Yee A. and Tsao L. (1981) Kinetics of silica polymerisation. *J. Colloid Interface Sci.* **84**, 379–402.

Yee N., Phoenix V. R., Konhauser K. O., Benning L. G. and Ferris F. G. (2003) The effect of cyanobacteria on Si precipitation kinetics at neutral pH: implications for bacterial silicification in geothermal hot springs. *Chem. Geol.* **199**, 83–90.

Zhang H., Chena B. and Banfield J. F. (2009) The size dependence of the surface free energy of titania nanocrystals. *Phys. Chem. Chem. Phys.* **11**, 2553–2558.

Associate editor: Christopher Kim